Corrosion Science 255 (2025) 113142

Contents lists available at ScienceDirect

Corrosion Science

journal homepage: www.elsevier.com/locate/corsci

Pb corrosion of ferritic/martensitic steels at 600–700 °C

Anisa Purwitasari [a], Renate Fetzer [a,*], Annette Heinzel [a], Ceyhun Oskay [a,b], Alfons Weisenburger [a], Georg Müller [a]

[a] Institute for Pulsed Power and Microwave Technology (IHM), Karlsruhe Institute of Technology (KIT), Hermann-von-Helmholtz-Platz 1, Eggenstein-Leopoldshafen 76344, Germany
[b] DECHEMA-Forschungsinstitut, Theodor-Heuss-Allee 25, Frankfurt am Main 60486, Germany

ARTICLE INFO

Keywords:
Corrosion
Liquid lead
Ferritic/martensitic steel
Aluminizing
Dissolution
Oxidation
Dissociation

ABSTRACT

This research investigates the corrosion behavior of three different ferritic/martensitic steels (P91, 1.4748, 1.4136) in liquid lead containing 2×10^{-7} wt% dissolved oxygen. Additionally, one of the steels (P91) is surface-aluminized by pack cementation prior to Pb exposure to explore the efficacy of an aluminide coating. The aim of this study is to explore the possibility to extend the use from a corrosion point of view of the selected F/M steels in liquid Pb up to 700 °C. To gain a better understanding of the corrosion behavior over time, exposure tests with three different durations up to 5000 h are performed. Post-exposure analysis demonstrates oxidation on all materials in the initial stage, followed by various differing scenarios specific for each material and exposure temperature. These range from oxidation with protective properties and selective Cr dissolution with intergranular Pb penetration to total dissolution.

1. Introduction

Ferritic/martensitic (F/M) steels offer several advantages when applied as structural material in future thermal energy storage (TES) systems and advanced nuclear fission and fusion technologies. Their low thermal expansion and good thermal conductivity help reduce thermal stress and deformation during temperature fluctuations. Moreover, F/M steels are cheaper and less susceptible to swelling and embrittlement under neutron irradiation compared with austenitic steels [1,2]. TES and nuclear systems operate at high temperatures, necessitating the use of effective heat transfer fluids. Heavy liquid metals are attractive heat transfer media, because they possess excellent thermal and physical properties to ensure optimal operational efficiency [3,4]. However, liquid metals are aggressive towards structural materials. The compatibility of F/M steels, particularly the 9Cr-1Mo alloys T91 and P91, in liquid lead (Pb) and lead-bismuth eutectic (LBE) under different temperatures and oxygen concentrations has been extensively studied. Most literature emphasizes the crucial role of dissolved oxygen content in the liquid metal, as it facilitates the in-situ formation of protective oxide layers that mitigate corrosion. In case of an insufficient oxygen content, dissolution of alloying constituents into the lead can occur, which increases the risk of liquid metal penetration into the steel matrix [5,6]. In contrast, an excessive oxygen level, especially at high temperature, can result in the growth of thick oxide layers, which reduce heat transfer and may break off due to accumulated stress in the scale. This can block flow channels and lead to further oxidation or liquid metal attacks. Heinzel et al. [7] reported that P91 developed a 36 μm thick multi-layer oxide scale, comprising an outward growing magnetite layer (14 μm), an inward growing Fe-Cr spinel layer (11 μm), and an inner oxidation zone (IOZ, 11 μm) after 2000 h exposure to liquid Pb with an oxygen concentration of 10^{-6} wt% at 550 °C. Similar oxidation behavior was also reported for T91 steel at 480–550 °C in oxygen saturated LBE [8,9] and in flowing (1 m/s) LBE with 10^{-6} wt% oxygen [10]. In the latter case, the overall oxide layer thickness reached 45 μm after 2000 h at 550 °C. Most studies are limited to exposure temperatures up to 550 °C, while literature on 600 °C and above, the temperature range anticipated for future TES systems, is scarce. Here, enhanced oxide growth and/or corrosion attack is expected on the surface of F/M steels and measures are sought to protect structural materials from excessive liquid metal corrosion/oxidation.

A slowly growing, thin alumina layer is recognized as one of the most stable and insoluble oxides in liquid metal. Surface treatments, such as alloying Al into the steel surface [11,12] and modifying FeCrAlY coatings on T91 [10], both by GESA treatment, have been shown to effectively promote the formation of an alumina layer on steel substrates with oxide thicknesses below 1 μm. Alumina-forming coatings have been

* Corresponding author.
E-mail address: renate.fetzer@kit.edu (R. Fetzer).

https://doi.org/10.1016/j.corsci.2025.113142
Received 6 May 2025; Received in revised form 20 June 2025; Accepted 23 June 2025
Available online 23 June 2025

applied to T91/P91 using different techniques, including physical vapor deposition (PVD), pulsed laser deposition (PLD), and diffusion coating via pack cementation [13–15]. Among these techniques, aluminide diffusion coating stands out due to its cost-effectiveness, industrial availability and, most importantly, the strong adhesion between the aluminide coating and the substrate. Deloffre et al. [15] reported that aluminized T91 demonstrated satisfying corrosion behavior in static LBE at temperatures up to 500 °C for up to 3000 h with oxygen contents as low as 10^{-9} wt%. However, at an elevated temperature of 600 °C and oxygen content in the range of 10^{-8}-10^{-9} wt%, the material exhibited heterogeneous corrosion behavior, with the formation of a corrosion layer marked by aluminum depletion and steel dissolution. It remains an open question whether an oxygen content higher than 10^{-8} wt% could enable the formation of a protective alumina layer and mitigate corrosion at 600 °C.

To date, there is a research gap regarding the corrosion resistance of P91 in liquid Pb at exposure temperatures of 600 °C and above. Similarly, the corrosion behavior of commercial F/M pump and valve steels, 1.4136 and 1.4748, has not yet been investigated in this temperature range. Therefore, this study aims at investigating and assessing the compatibility of these materials in liquid Pb at the temperatures 600 and 700 °C. For the exposure tests, an oxygen content of 2×10^{-7} wt% was selected, which allows formation of Fe spinel, Cr-oxides, and Al-oxides, while avoiding oxidation of Pb and excessive oxidation of the steel surfaces. To gain a better understanding of the corrosion behavior over time, three different exposure periods, extending up to 5000 h, have been selected. In addition, the efficacy of an aluminide coating applied to P91 by pack cementation is assessed under the same exposure conditions.

2. Materials and methods

2.1. Materials

Three F/M steels of different composition were selected for the exposure tests. Table 1 presents their chemical composition. P91 is a commercial 9 wt% Cr martensitic steel and available at the KIT inventory. Fig. 1a shows the initial microstructure of P91 after etching. A martensitic microstructure with a grain size of 30–50 μm is observable. In this study, P91 was exposed to liquid Pb in two different conditions: as received and aluminized. The pump and valve steel 1.4748 with ~17–18 wt% Cr and the ferritic pump steel 1.4136 with 27–30 wt% Cr were provided by the company KSB, Germany. The steel 1.4748 was delivered in annealed condition. Its microstructure is characterized by a martensitic matrix interspersed with Cr-rich carbide precipitates (Fig. 1b). The microstructure of 1.4136 is shown in Fig. 1c. Ferritic grains with an average size of 55 μm are visible, along with CrFeMo complex carbides primarily located at the grain boundaries. Some Al-nitride precipitates and pores are also found.

The materials were cut into coupons measuring 27 × 8×2 mm, except for 1.4748, which was cut into half-cylinders with a diameter of 19 mm and a height of 10 mm. The samples were then polished with #1200 SiC paper and cleaned with ethanol prior to the corrosion tests. High purity lead bars (99.995 %), supplied by HMW Hauner GmbH Co. KG, were used. The lead bars were melted and poured into alumina crucibles, which were subsequently placed on a nickel-based tray to allow multiple samples to be loaded in one test series.

Aluminide coatings were deposited on P91 using the industrially established method of pack cementation at 1000 °C for 1 h. P91 samples were embedded inside alumina retorts in a pack mixture consisting of 1.5 wt% Al as the master alloy, 1 wt% NH_4Cl as the activator, and Al_2O_3 (rest) as the inert filler and, thereafter, placed inside a horizontal test rig equipped with a quartz glass tube. Prior to the heating, the tube was evacuated using a vacuum pump and filled with Ar three consecutive times. Thereafter, the heating and the coating deposition were conducted under flowing Ar/5 vol% H_2. After the dwell time of 1 h, the samples were cooled down in the furnace followed by their removal from the retorts and cleaning in an ultrasonic acetone bath. Further details on the coating manufacturing process can be found in [16,17]. The selection of such a high coating manufacturing temperature originates from the formation of brittle Al-rich intermetallic phases such as Fe_2Al_5 at inferior coating temperatures, jeopardizing the mechanical behavior of components [18,19]. Despite the possibility of performing the coating manufacturing at a temperature matching the austenitization temperature of P91, the process requires constant Ar/H_2 flow in a glass tube and hence cannot be coupled with a fast cooling process to restore the martensitic microstructure. As a result, it is accompanied by the requirement of a post-coating heat treatment for F/M steels as reported in [20]. After the coating deposition, aluminized P91 samples were heat-treated with a two-step process including the austenitization at 1050 °C for a soaking time of 30 mins, after which the samples were removed from the furnace to enable fast air-cooling, followed by a tempering treatment at 770 °C for 1 h, both undertaken in a muffle furnace to restore the tempered martensitic microstructure. More details on the heat treatment of P91 steel can be found in [21,22]. It should be noted that during the heat treatment process undertaken to restore the original P91 microstructure, the aluminide coating microstructure was possibly altered before the exposure in molten Pb due to the formation of an Al-rich oxide scale in still air and interdiffusion with the substrate as highlighted in [23]. Owing to the necessity of a heat treatment to restore the original microstructure and thus the high creep strength of the alloy, further sections will refer to the heat-treated aluminized P91 as the initial condition.

2.2. Corrosion tests

The stagnant corrosion test was carried out at the COSTA facility at KIT under controlled oxygen concentration [11]. The facility includes a furnace with a quartz glass tube inside, where a nickel-based tray containing alumina crucibles filled with liquid Pb is placed. One end of the quartz glass tube is closed, while the other remains open and can be sealed with a removable cap equipped with gas inlet and outlet ports. To regulate oxygen levels within the quartz-glass tube and consequently dissolved oxygen in liquid Pb, a continuous flow of a gas mixture with a defined H_2/H_2O ratio was used. Samples were loaded once the oxygen partial pressure in the system was conditioned to the target value and equilibrium was achieved between the gas phase and the liquid Pb. A conditioned glove box was employed during sample loading and unloading to prevent unexpected oxygen ingress. The oxygen partial pressure was measured at the gas outlet, allowing for calculation of the concentration of dissolved oxygen in liquid Pb based on oxygen saturation data [24]. The target oxygen content was 2×10^{-7} wt%, which was monitored throughout the entire test period, see Fig. 2. The tests were conducted at two temperatures, 600 and 700 °C, for durations of 1000 h, 2000 h, and 5000 h. In the tests at 600 °C, the achieved oxygen content varied between 1×10^{-7} wt% and 2×10^{-7} wt%, while the

Table 1
Nominal composition of F/M steels in wt%.

Material	C	N	S	Cr	Ni	Si	Mn	Mo	V	Nb	Fe
1.4903 (P91)	0.08–0.12	0.03–0.07	≤ 0.02	8.0–9.5	≤ 0.4	≤ 0.5	0.3–0.6	0.85–1.05	0.18–0.25	0.06–0.1	bal.
1.4748	0.8–0.9		0.03	16.5–18.5		≤ 1.0	≤ 1.5	2.0–2.5	0.3–0.6		bal.
1.4136	0.5–0.9		0.03	27.0–30.0		≤ 2.0	≤ 1.0	2.0–2.5			bal.

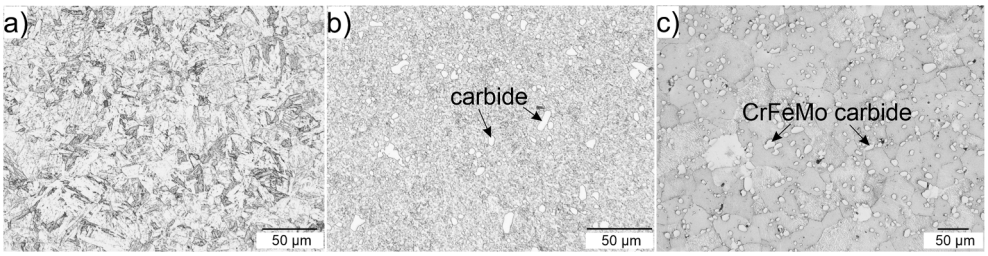

Fig. 1. Bulk microstructure of original materials a) P91, b) 1.4748, and c) 1.4136. Shown are optical microscope images after etching.

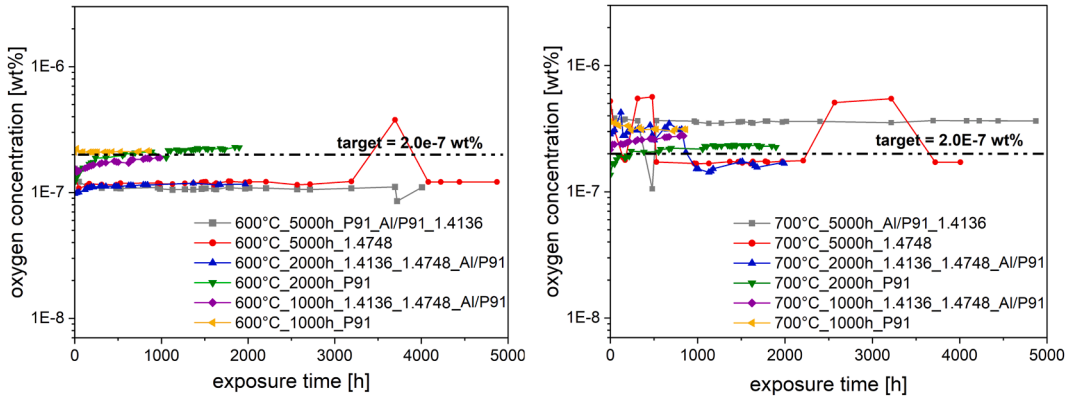

Fig. 2. Concentration of oxygen dissolved in liquid Pb during the exposure tests. Left: experiments at 600 °C, right: 700 °C experiments.

values ranged from 1×10^{-7} wt% to 5×10^{-7} wt% in the tests at 700 °C.

2.3. Characterization methods

After removal from the COSTA facility, the samples were cooled to room temperature under a controlled atmosphere and then cut into two parts. The first part of each sample was used for cross-sectional analysis and embedded in resin without any prior cleaning. The samples were metallographically prepared by grinding with SiC paper until 4000 grit and polishing with a diamond suspension down to 1 µm. Prior to cross-sectional analysis, the samples were sputtered with Au to improve the electrical conductivity. Scanning electron microscopy (SEM, Zeiss LEO 1530 VP), equipped with an energy-dispersive X-ray spectrometer (EDS) and electron backscatter diffraction (EBSD), was employed for the analysis. In addition to the samples tested after exposure, the original pre-exposure samples were prepared for cross-section analysis to investigate the initial microstructure. To reveal the microstructure, some of the exposed samples, along with the original sample, were etched using a mixture of 200 ml ethanol, 25 ml hydrochloric acid, 25 ml nitric acid, and 3 g picric acid. Microstructural images were then acquired using an optical microscope (Olympus BX60M). For X-ray diffraction (XRD, Seifert 3003 PTS) analysis, the second part of each sample was cleaned from adherent lead by immersing into a mixture of acetic acid, hydrogen peroxide, and ethanol in a 1:1:1 ratio, followed by rinsing with distilled water and ethanol. This analysis aimed at identifying the coating structure deposited after the pack-cementation process and the corrosion products formed during exposure. In addition, EBSD investigation was performed to reveal microstructural changes in the exposed P91 samples. Following the described preparation protocol, the sample cross-sections were further polished with a 1/4 µm diamond suspension, then polished with a vibratory polisher using a colloidal silica suspension for 4 h.

3. Results and discussion

3.1. Martensitic steel P91

Fig. 3a shows the cross-sectional image of P91 steel after 1000 h of exposure in liquid Pb at 600 °C. A multi-layer oxide structure, consisting of an outer and an inner oxide layer, has developed on P91. According to the EDS line scan in Fig. 3b and EDS elemental mapping shown in Fig. 3c, the 10 µm thick outer oxide layer is mainly composed of Fe and O, and it is identified as Fe_3O_4 (magnetite) by the XRD results, see Fig. 4. However, the outer magnetite layer appears porous and exhibits local delamination, allowing liquid Pb to penetrate (see Pb mapping in Fig. 3c). The inner oxide layer, with a thickness of 8–12 µm, is confirmed as Fe-Cr spinel. Liquid Pb is also detected within the inner Fe-Cr spinel, indicating that the spinel is not completely protective against liquid Pb penetration. According to the line scan in Fig. 3b and the mapping result in Fig. 3c, a Cr-rich spinel accompanied with Si-enrichment is observed at the interface between the inner oxide layer and the bulk. Below the continuous spinel layer, some small oxide roots are observed. The oxide structures identified after 1000 h are very similar to those reported in another study for exposure at 550 °C for 2000 h in liquid Pb with an oxygen content of approximately 10^{-6} wt% [7].

Fig. 3d shows a representative cross-sectional image of P91 after 2000 h of exposure, on which a continuous Fe-Cr spinel layer with a thickness of 2–3 µm can be seen. No magnetite layer is detected. This can be interpreted in two ways: either no magnetite was formed at all or the previously formed magnetite layer has completely spalled off. It is notable that the 2000 h sample exhibits a lower thickness of the Fe-Cr spinel layer compared with the 1000 h sample despite the longer exposure time. This discrepancy could be attributed to a slightly lower oxygen concentration in the liquid Pb at the beginning of the 2000 h exposure (see Fig. 2). The initially lower oxygen concentration could also be responsible for the formation of Cr-rich Fe-Cr spinel instead of Fe-rich oxide, see line scan in Fig. 3e versus Fig. 3b. Cr-rich spinel is typically denser, thus reducing the diffusion of Fe and O. In addition to the slower growth of the spinel, this could also explain the absence of

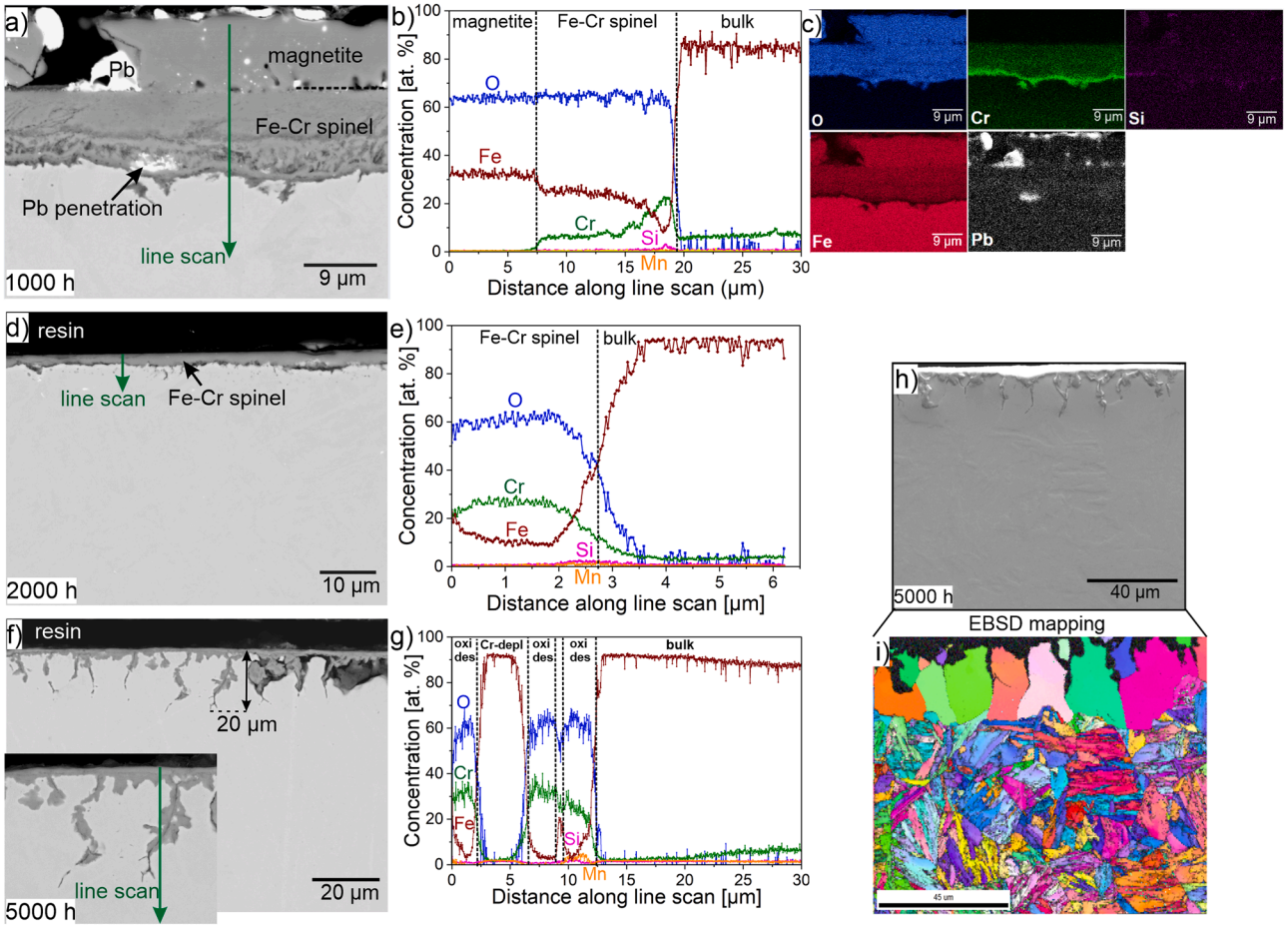

Fig. 3. P91 samples after exposures in liquid Pb at 600 °C. a) BSE image after 1000 h, b) corresponding line scan result, c) corresponding EDS elemental mapping result, d) BSE image after 2000 h, e) corresponding line scan result, f) BSE image after 5000 h, g) corresponding line scan result, h) SE image after 5000 h, i) corresponding EBSD phase mapping result.

magnetite. Furthermore, Pb penetration is not found, which confirms the higher protectiveness of the spinel layer. Similar to the 1000 h sample, the spinel layer is enriched in Si at the interface to the bulk and some oxide roots are observed below the spinel layer, indicating the beginning of inner oxide formation.

After 5000 h of exposure, a continuous oxide scale and an inner oxide zone up to 20 µm in depth is observed on the martensitic steel P91 (Fig. 3f). The oxide scale is verified as Cr-rich Fe-Cr spinel by the line scan (Fig. 3g) and XRD results, see Fig. 4, while the inner oxide is identified as Cr_2O_3, with Si and Mn enrichment at the tips of the oxide branches (Fig. 3g). The Cr content of the spinel is similar or even slightly higher than on the 2000 h sample, suggesting slow growth of a dense and protective scale without magnetite formation. As in the beginning of the 2000 h exposure, also the 5000 h test had a slightly lower oxygen concentration. No liquid Pb is detected, which confirms that the oxides provide effective protection against liquid Pb corrosion. The oxidation of Cr results in a Cr depletion of the steel matrix in the vicinity of the oxides, see Fig. 3g. EBSD phase mapping (Fig. 3i) reveals ferritization of the martensite structure down to a depth of 30–40 µm, most probably caused by the Cr depletion in this region.

The corrosion behavior of P91 at 700 °C is presented in Fig. 5. After 1000 h of exposure, an inward-growing oxide is found, progressing presumably along the grain boundaries to a depth of 10 µm (Fig. 5a). According to the elemental mapping in Fig. 5c, the oxides are primarily composed of Cr and O, which corresponds well with Cr_2O_3 as identified from the peaks in the XRD pattern in Fig. 4. Additionally, the surface-near oxides contain some Fe, which agrees with the XRD peaks identified as Fe-Cr spinel, while the oxides at the interface to the steel are enriched in Si. Below the oxidation zone, EBSD mapping shows ferritization, see Fig. 5b, presumably due to the slight Cr depletion observed in this region (Fig. 5c). Additionally, Mn-sulfide precipitates are formed along the grain boundaries in the ferrite zone, see Fig. 5d for the result of an EDS line scan through one of these precipitates. Note that Mn has fairly high affinity for sulfur. Sulfur in this case may be present as an impurity in the liquid Pb or originate from the substrate, as sulfur may also be present in the steel, see Table 1. Besides Cr depletion, the EDS mapping of Cr in Fig. 5c also indicates the dissociation of Cr-rich carbides, as P91 steel is known to contain carbides, particularly of type $M_{23}C_6$ at the grain boundaries [25].

The depth of the inward-growing intergranular oxidation increases with increasing exposure time, reaching 35 µm after 2000 h and 110 µm after 5000 h (see Fig. 5e and f). In these locations with deep intergranular oxidation, the Mn-sulfides observed along grain boundaries in the surface-near region after 1000 h exposure have disappeared. However, in regions where the inner oxidation is less deep, the MnS precipitates are still present after 2000 h and 5000 h exposure. A noticeable depletion of Cr is observed within the oxidation zone after 5000 h (elemental mapping in Fig. 5g), which is attributed to the preferential oxidation of Cr.

Although lead penetration into the oxidized region is observed for all three exposure times, no Pb penetration into the bulk of P91 is found after the tests at 700 °C.

A summarized assessment is presented in Table 2, providing an overview of the development of the corrosion behavior of P91 over the exposure times at both temperatures. At 600 °C, a continuous Fe-Cr spinel layer grows, the Cr content of which depends on the exact

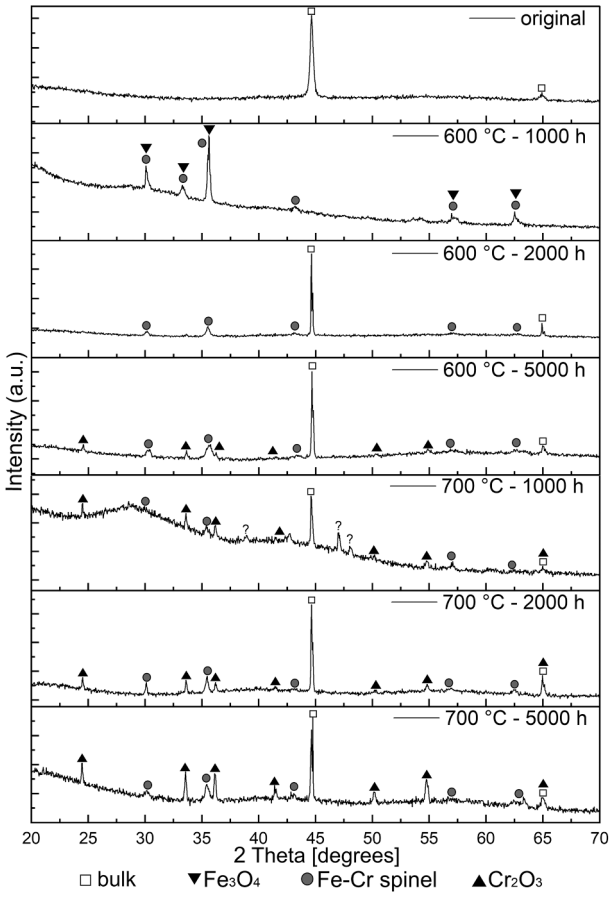

Fig. 4. XRD results of P91 before and after exposures at 600 °C and 700 °C for different exposure times.

exposure conditions, i.e., the concentration of oxygen dissolved in the liquid lead. Only the sample exposed for 1000 h, which was exposed to the highest oxygen content compared to the longer durations, shows formation of outward-growing magnetite and Fe-Cr spinel with a relatively low Cr content of ~6 at%. However, these oxides are not protective against penetration of Pb into the oxide scale. In contrast, the thinner Fe-Cr spinel formed after 2000 h and 5000 h exposure, with higher Cr contents of ~27 at% and ~32 at%, respectively, is dense and effectively protects against Pb penetration. It is also worth noting that the oxygen content of the 2000 h exposure was slightly higher than that for the 5000 h exposure. This demonstrates that the lower the oxygen content is, the higher is the Cr content of the spinel, the thinner is the spinel layer formed, and the more protective and stable it is. Inward-growing selective oxidation of Cr along grain boundaries is observed in all cases, no matter what the Cr content and density of the spinel is.

At 700 °C, the thin Fe-Cr spinel formed at the surface is unstable and becomes discontinuous in some areas. Liquid Pb penetrates the inward-growing oxide. The inward-growing oxidation along grain boundaries proceeds faster than at 600 °C.

In addition to the selective oxidation of Cr, the oxides are enriched in Si at the oxidation front respectively at the tips of the inward-growing oxide branches, which has been observed previously [26–28]. Neither Pb penetration into the bulk material nor selective dissolution of Cr are observed in any of the tests, which suggests that the oxides grown on P91 are protective against lead corrosion at both temperatures.

Table 2
Summarized assessment of P91 after exposures at 600 °C and 700 °C.

	600 °C			700 °C		
	1000 h	2000 h	5000 h	1000 h	2000 h	5000 h
Continuous spinel layer	8–12 μm	2–3 μm	< 1 μm	-	-	-
Inward-growing Cr-oxide	5 μm	3 μm	20 μm	10 μm	35 μm	110 μm
Pb penetration into oxide	10 μm	-	-	2 μm	8 μm	14 μm
Pb penetration into bulk	-	-	-	-	-	-
Selective Cr dissolution	-	-	-	-	-	-

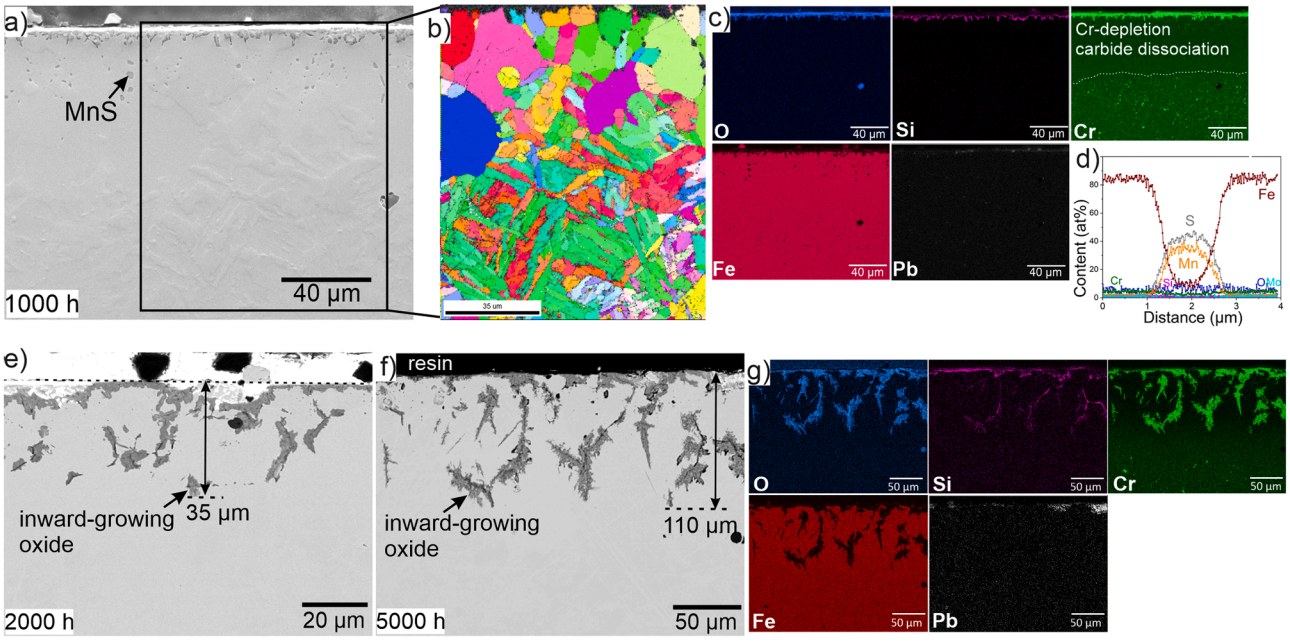

Fig. 5. P91 samples after exposures at 700 °C. a) SE image after 1000 h, b) corresponding EBSD phase mapping and c) EDS elemental mapping result, d) result of line scan through MnS precipitate, e) BSE image after 2000 h, f) BSE image after 5000 h, g) corresponding EDS elemental mapping result.

3.2. Steel 1.4748

Fig. 6 presents the bulk microstructure of 1.4748 prior to and after the Pb exposure tests. It is evident that the number of Cr-carbides decreases after exposure at 700 °C, while hardly any change in microstructure is observed after exposure at 600 °C. The reduction in the number of Cr-carbides at 700 °C is attributed to the coarsening of the carbides, which occurs more rapidly at elevated temperatures due to the accelerated diffusion of alloying elements.

After 1000 h of exposure at 600 °C in liquid Pb, the surface of steel 1.4748 exhibits a continuous 3–5 μm thick Fe-Cr-Mn spinel layer, which shows a heterogeneous composition and is locally interrupted by liquid Pb penetration with depths up to 30 μm, in one location even 70 μm (Fig. 7a). The Pb penetration is accompanied by Cr depletion in the matrix (see line scan in Fig. 7b), disappearance of the Cr-carbides due to carbide phase dissociation, and formation of small Mn-rich precipitates (see also EDS elemental mapping in Fig. 7d). The Cr depletion is attributed to oxide formation and to selective dissolution via the leaks in the spinel layer. A possible explanation for the discontinuity of the spinel layer could be local defects in the previously formed spinel layer or microstructural inhomogeneities of the bulk material such as surface-near carbides, which may inhibit the outward diffusion of oxide-forming elements, thereby preventing oxide re-formation in certain areas.

As the exposure duration increases, the previously formed oxide layer disappears, leading to an intensification of the extent and severity of the corrosion attack. After 5000 h, all pre-formed oxides and the original surface of 1.4748 have totally disappeared due to detachment or dissolution (Fig. 7c). Additionally, local Pb penetration up to 110 μm deep and selective dissolution of Cr in the vicinity of the penetrated Pb are observed. The sample exposed for 2000 h showed a totally different corrosion behavior due to a fault in the exposure test and was therefore not further considered for this study.

The corrosion characteristic observed on the 1.4748 samples exposed at 700 °C is presented in Fig. 8. The steel surface shows total dissolution/detachment already after 1000 h of exposure, see Fig. 8a. The liquid Pb adherent to the steel surface contains remains of the dissolved steel. Local remnants of previously formed Cr-, Si-rich oxide are found on the steel surface, which are ineffective in providing protection against corrosion. The corroded surface is additionally penetrated by Pb up to a depth of further 30 μm. Based on the EDS elemental mapping shown in Fig. 8b, the Cr-carbides have dissociated to a depth of about 20 μm. Since no significant change in Cr concentration is detected in the corresponding matrix, this corresponds to an overall reduction of the Cr content, which is attributed to selective dissolution of Cr into the adjacent liquid Pb. Complex precipitates rich in Mn and S are found in the Cr-depleted region of the steel. Similar corrosion behavior is observed for the sample exposed for 2000 h, see Fig. 8c.

On the sample exposed for 5000 h at 700 °C, a more heterogeneous corrosion behavior is evident, see Fig. 8d. In some areas, inward-grown oxide is present. EDS elemental mapping (Fig. 8e) reveals selective oxidation of Cr and Mn, while a metallic Fe-rich phase and Pb penetration are observed between the oxides. The oxides are enriched in Si at the interface to the bulk material. Pb penetration into the bulk is not observed in the areas with inward-grown oxide. However, as observed next to the oxides, the inward-grown oxide is not stable but becomes unstable and detaches. This is believed to be caused by the heterogeneous structure of the oxide mixed with the metallic phase, the latter being susceptible to dissolution in Pb. The only remains of the previously formed oxide are some Si-rich oxide islands at the interface to the bulk, which is consistent with the behavior observed after 1000 h and 2000 h. In regions with dissolved oxide, total dissolution of the steel is observed. Additionally, the Cr-rich carbides have dissociated near the surface due to selective dissolution of Cr, and Mn-, S-rich complex precipitates have formed in this region. Responsible for the obviously better stability of the inward-growing oxide on the sample exposed for 5000 h could be the temporarily higher oxygen concentration in liquid Pb during the 5000 h test compared with the shorter exposure tests (Fig. 2).

The behavior of 1.4748 over different exposure times and temperatures is summarized in Table 3. At both temperatures, corrosion of 1.4748 is characterized by an initial inward-growing oxidation of Cr and Mn, followed by dissolution/detachment of the unstable oxidation region and total dissolution of the steel. Steel dissolution is accompanied by local penetration of Pb and selective dissolution of Cr. The latter results in the dissociation of the Cr-carbides and the formation of Mn-rich complex precipitates in surface-near regions and surrounding the local penetrations of Pb. The range of the Cr depletion is larger at the higher temperature due to the higher diffusion rates. The dissociation of surface-near Cr-carbides due to selective dissolution of Cr during exposure to liquid Pb-Bi eutectic was recently investigated for T91 [29]. It was proposed that the Cr dissolution leads to a depletion of Cr in the matrix, which destabilizes the Cr-carbide phase and results in the respective dissociation.

A possible explanation for the instability of the Fe-Cr-Mn spinel layer grown on 1.4748 at 600 °C could be the heterogeneity in its composition. Such heterogeneity was not observed for the Cr-rich spinel grown on P91 (Fig. 3). Since the Cr contents of P91 (~9 wt%) is similar to the Cr concentration in the matrix of 1.4748 (~10 wt%), the heterogeneity and inferior stability of the oxide scale grown on 1.4748 might be caused by the higher Mn content in 1.4748. It was reported previously that the presence of Mn in F/M steels in concentrations around 1–2 wt% has a significant effect on the high temperature oxidation resistance [30–32]. With contents below ~1 wt%, Mn reduces the oxidation rate and leads to more compact oxide scales [30], while Mn in higher concentrations increases the oxidation rate and leads to less uniform, discontinuous, and less protective oxide scales [32], in particular if the Mn content exceeds the Si content [31]. The resulting scale is expected to be more susceptible to dissolution when exposed to liquid Pb.

At 700 °C, the key feature of corrosion of 1.4748 observed in this study is the formation of an inward-growing oxidation region with incomplete oxidation (selective oxidation of Cr and Mn). The incomplete oxidation is responsible for the instability and dissolution of the entire oxidation region into the adjacent Pb. The only remnants of the oxidation region after its dissolution are Si-rich oxides previously formed at the interface to the steel, indicating their higher stability and good adherence to the steel.

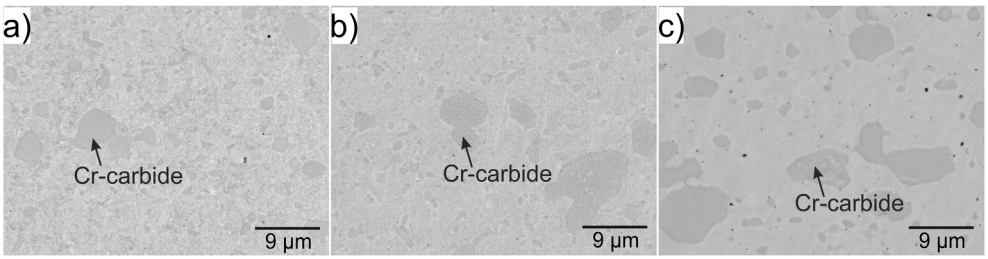

Fig. 6. Bulk microstructure of 1.4748. a) BSE image of initial state after etching, b) BSE image after 5000 h exposure at 600 °C (unetched), c) BSE image after 5000 h exposure at 700 °C (unetched).

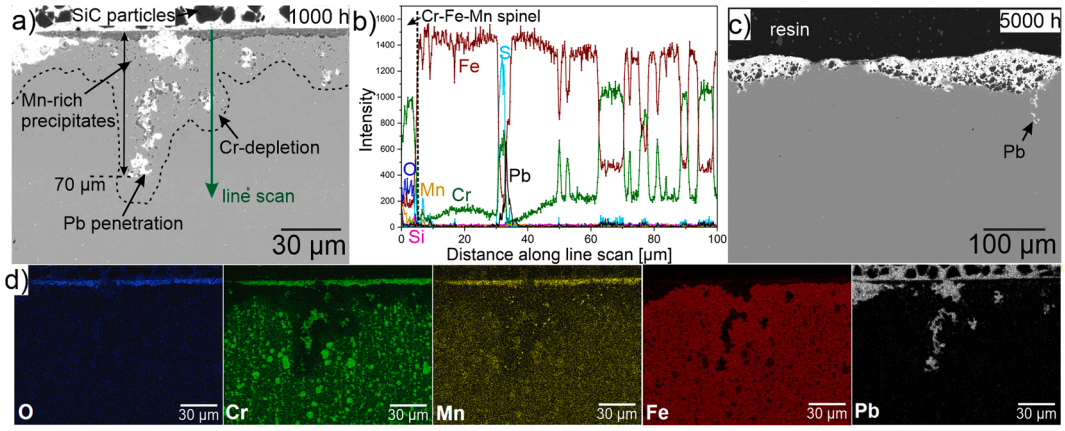

Fig. 7. 1.4748 samples after exposures at 600 °C. a) BSE image after 1000 h, b) corresponding line scan result, c) BSE image after 5000 h, d) EDS elemental mapping result of a). Note that the dark regions in Pb are SiC particles, which were embedded in the Pb during the grinding preparation process using SiC abrasive paper.

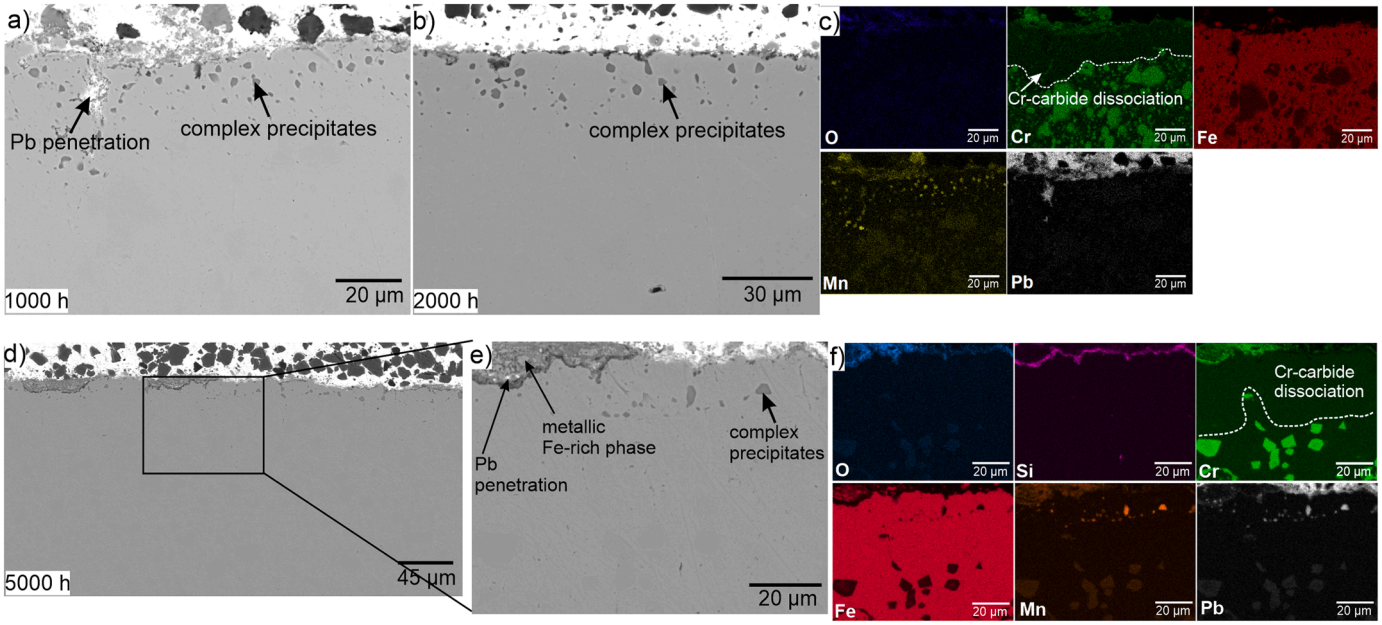

Fig. 8. 1.4748 samples after exposures at 700 °C. a) BSE image after 1000 h, b) corresponding EDS elemental mapping, c) BSE image after 2000 h, d) BSE image after 5000 h, e) zoom to location marked in d), f) corresponding EDS elemental mapping.

Table 3
Summarized assessment of 1.4748 after exposures at 600 °C and 700 °C.

	600 °C		700 °C		
	1000 h	5000 h	1000 h	2000 h	5000 h
Inward-growing oxide	3–5 µm	-	remains	remains	40 µm
Total dissolution	-	✓	✓	✓	✓
Pb penetration	30 (70) µm	110 µm	30 µm	30 µm	60 µm
Selective Cr dissolution	✓	✓	✓	✓	✓
Range of Cr depletion	10 µm	10 µm	20 µm	25 µm	40 µm

3.3. Ferritic steel 1.4136

The change of the bulk microstructure of 1.4136 due to exposure at elevated temperature is shown in Fig. 9. After 5000 h of exposure at 600 °C, the steel exhibits an elongated chromium-rich phase (bright grey) along the ferrite grain boundaries, accompanied by Cr-depleted ferrite solid solution (medium dark grey), cf. Fig. 9b. EDS point measurements on the Cr-rich phase indicate a composition of 55 at% Fe, 36.5 at% Cr, and 4.3 at% Mo, suggesting the presence of a Cr-rich σ-phase. It is noticed that the CrFeMo complex carbides (dark grey) are preferentially surrounded by the σ-phase. The brightest phase formed at the ferrite grain boundaries within the σ-phase is identified as Mo, Si-rich carbide precipitates, also known as the χ-phase [33]. Additionally, elongated Cr-nitride precipitates are formed. After exposure at the higher temperature of 700 °C (Fig. 9c), the χ-phase is not observed and the proportion of the σ-phase is lower than at 600 °C. Unlike at 600 °C, the σ-phase at 700 °C is not interconnected. The Cr-nitride precipitates are formed at both temperatures, while Al-nitrides are observed both prior to and after the exposures.

Regarding the corrosion behavior, Fig. 10a shows that after 1000 h of exposure at 600 °C, the 1.4136 steel is covered by a thin (~0.7 µm) continuous Cr-rich spinel layer. Locally, the spinel is thicker and shows inward growing oxide roots up to 5 µm deep. As shown in the line scan (Fig. 10b), the Cr-rich spinel also contains Fe, Si, and Mn. No liquid Pb penetration is observable. However, after 2000 h of exposure, intergranular liquid Pb penetration is observed in the bulk material (Fig. 10c), with only localized oxide remaining. This suggests that the previously formed Cr-rich spinel is unstable during prolonged exposure and does not re-form thereafter. As shown in Fig. 10d, significant

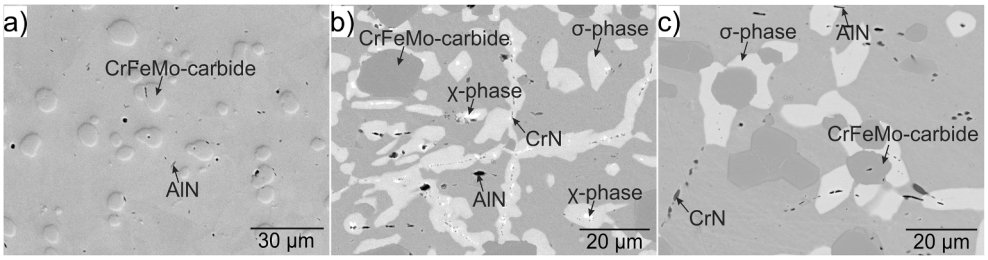

Fig. 9. Bulk microstructure of 1.4136. a) SE image at initial state after etching, b) BSE image after 5000 h of exposure at 600 °C (unetched), c) BSE image after 5000 h of exposure at 700 °C (unetched).

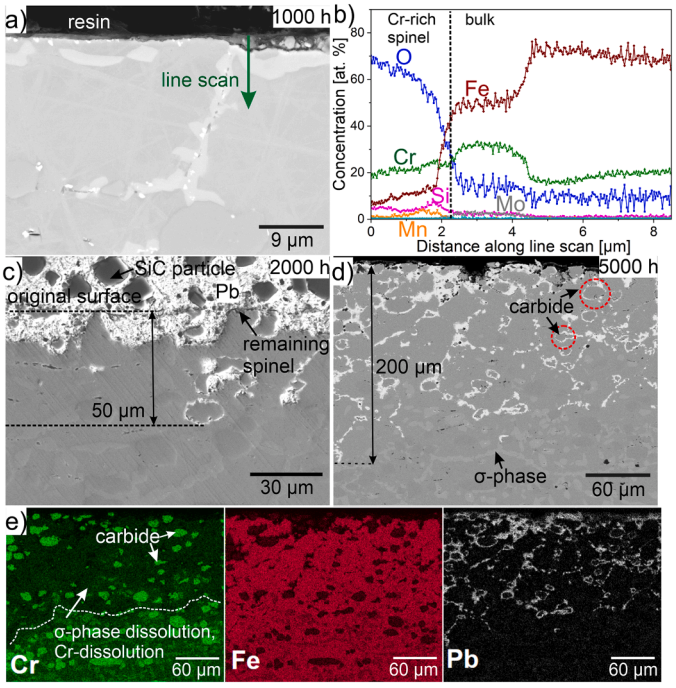

Fig. 10. 1.4136 sample after exposures at 600 °C. a) BSE image after 1000 h, b) corresponding line scan result, c) SE image after 2000 h, d) BSE image after 5000 h, e) corresponding EDS elemental mapping result.

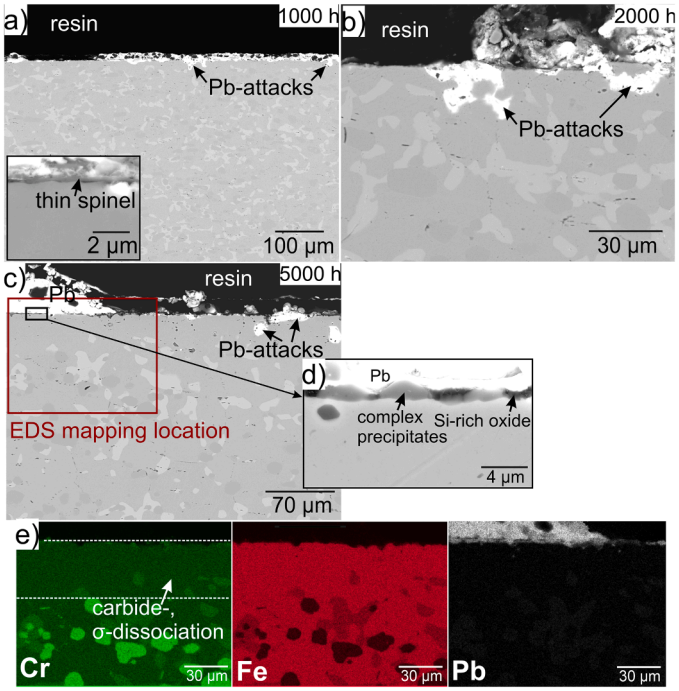

Fig. 11. 1.4136 samples after exposures at 700 °C. a) BSE image after 1000 h, b) BSE image after 2000 h, c) BSE image after 5000 h, d) higher magnification detail of image c), e) EDS elemental mapping of the location marked in c).

intergranular penetration of liquid Pb progresses within the bulk of the steel, reaching a visible depth of 200 µm after 5000 h of exposure at 600 °C, making the outermost grains susceptible to detachment. No remains of an oxide layer are found. Notably, the σ-phase, which is typically found along the grain boundaries, is no longer detectable in the corroded region. This indicates that the absence of the spinel layer leads to the dissolution of the σ-phase near the surface, which facilitates the intergranular liquid Pb penetration. In contrast, the CrFeMo carbides appear to remain intact against Pb corrosion, despite being directly surrounded by penetrated Pb (see red marks in Fig. 10d). Furthermore, EDS elemental mapping (Fig. 10e) and point measurements indicate a depletion of chromium in the corroded matrix, with its concentration decreasing from ~20 at% in the bulk to 10 at% in the corroded region. This Cr depletion is attributed to selective dissolution into the adjacent liquid Pb.

Fig. 11a shows a representative cross-sectional image of the 1.4136 steel after 1000 h of exposure at 700 °C, revealing a laterally extended region with liquid Pb penetration, locally up to 20 µm deep, and a small corrosion-protected region. The high magnification image in the inset of Fig. 11a shows a very thin (~200 nm) spinel on the protected area. The bulk microstructure with CrFeMo-carbides and σ-phase extends to the sample surface both in the region with Pb penetration and in the protected area. With longer exposure time, the corrosion attack increases and the Pb penetration reaches a maximum depth of 35 µm after 2000 h (Fig. 11b) and of 70 µm after 5000 h. Nevertheless, there are still small areas free of liquid Pb penetration, where thin Si-rich oxide islands are found locally on the surface, alongside complex precipitates rich in Mn and S (Fig. 11d). After 2000 h, CrFeMo-carbides and σ-phase still exist next to the surface. However, after 5000 h of exposure, both the CrFeMo-carbides and the Cr-rich σ-phase have dissociated down to a depth of 30 µm (Fig. 11e) without significant change of the Cr content in the matrix, indicating selective dissolution of Cr into liquid Pb.

Table 4 summarizes the corrosion behavior of 1.4136 in liquid Pb. At both 600 and 700 °C, the steel is initially protected by formation of a thin Cr-rich spinel layer on its surface. After the initial protection, however, Pb penetrates locally into the steel and dissolves the Cr-rich σ-phase. Depending on the exposure temperature, a distinct corrosion pattern evolves. This pattern is directly related with the bulk microstructure shown in Fig. 9. At 600 °C, the Cr-rich σ-phase forms an interconnected network along the grain boundaries. During Pb exposure, this network of σ-phase is dissolved and penetrated by Pb. As a result, rather deep intergranular corrosion is observed. The CrFeMo carbides that are in direct contact with penetrated Pb are stable and remain intact, demonstrating their high stability at 600 °C. A possible explanation could be that the penetrated Pb is already saturated in Cr due to the dissolution of the σ-phase. At 700 °C, the σ-phase does not

Table 4
Summarized assessment of 1.4136 after exposures at 600 °C and 700 °C.

	600 °C			700 °C		
	1000 h	2000 h	5000 h	1000 h	2000 h	5000 h
Continuous spinel layer	0.7 μm	disc.	disc.	disc., 0.2 μm	disc.	disc.
Inward-growing oxide	5 μm	-	-	-	-	-
Pb penetration	-	50 μm	200 μm	20 μm	35 μm	70 μm
Selective Cr dissolution	-	✓	✓	✓	✓	✓

form an interconnected network but clearly separated patches. In this case, when a patch of σ-phase located at the sample surface is dissolved and penetrated by Pb during exposure, the corrosion cannot proceed easily via a path susceptible to corrosion. As a consequence, Pb penetration remains rather local, with corrosion depths lower than at 600 °C.

At both exposure temperatures, selective dissolution of Cr occurs and results in microstructural changes in surface-near regions. Both the σ-phase and the CrFeMo carbides are destabilized and dissociate at 700 °C.

3.4. Aluminized P91

Fig. 12a presents an SEM image of the pack-aluminized P91 prior to Pb exposure. The deposited coating is approximately 150 μm thick and comprises an outer aluminide layer and a ferritic interdiffusion zone (IDZ). The average Al-concentration in the outer layer is measured to be about 34 at% (Fig. 13a). The XRD analysis in Fig. 14 confirms the FeAl structure, indicating that the outer layer is FeAl with B2-order. Kirkendall voids are evident within the coating, mainly in the outer B2-FeAl layer. The corresponding unetched image at the bottom of Fig. 12a clearly shows the formation of an α-Al_2O_3 (corundum) layer on the coating and within the Kirkendall voids, which very likely occurred due to the imbalanced diffusion fluxes of Al and Fe in opposite directions during the heat treatment after the pack cementation process as highlighted in [34]. Additionally, needle-shaped Al-nitride precipitates are observed in the lower region of the ferritic IDZ, which is in line with the findings by Bates et al. in [23]. P91 contains nitrogen, which diffuses outward during the aluminizing process and is possibly rejected from the newly formed Al-enriched ferritic matrix, forming Al-nitride due to the aluminum's high affinity for nitrogen. The Al-nitrides are found preferentially along a line that marks the interface between IDZ and bulk after the pack cementation treatment but prior to subsequent heat treatment. During the heat treatment, the IDZ increased in thickness and AlN precipitated preferentially at the former interface.

Fig. 12b-c presents the etched images of the aluminized P91 samples after 5000 h exposure at 600 °C and 700 °C, respectively. The results from the 1000 h and 2000 h exposures at both temperatures exhibit similar and consistent behavior. No significant growth of the outer layer and the IDZ is observed; their thicknesses remain unchanged. However, the Al concentration in the coating drops and its profile across outer layer and IDZ becomes flatter, with a significant Al content in the bulk below the IDZ in particular after exposure at 700 °C, see Fig. 13b-c. After 5000 h of exposure at 600 °C, the Al concentration in the outer layer decreases to ~20 at%, while ~16 at% Al remain after 5000 h at 700 °C. The flattening of the Al concentration profile is caused by inward diffusion of Al, the consumption of Al by oxide formation on the sample surface and within the Kirkendall voids (see below), and diffusion of Fe from the bulk into the coating, with all three processes occurring faster at the higher temperature. The decrease in Al concentration in the outer layer leads to a gradual transformation of the B2-FeAl phase into a still Al-rich α-solid solution, especially visible after 5000 h at 700 °C, which is confirmed by the XRD results presented in Fig. 14 (peaks denoted FeCr).

In addition to the flattening of the concentration profiles, an increased amount of Kirkendall voids is observed in the coating after the Pb exposures, with the quantity rising with increasing exposure time and temperature. Additionally, Cr-rich, Mo-containing carbides and Al-nitrides are formed in the lower part of the IDZ and at the transition to the bulk P91. The extent of AlN precipitates at the transition to the bulk is higher after exposure at 700 °C due to the higher nitride formation potential at higher temperature and the higher Al concentration below the IDZ.

Regarding the corrosion behavior of aluminized P91, no liquid Pb penetration or internal oxidation is detected in the bulk at either temperature (Fig. 12b-c). This is in line with an earlier investigation and other studies reporting high corrosion resistance of corundum layers against liquid Pb corrosion [35–37]. Liquid Pb penetrates very locally into the Kirkendall voids, but the coating and the bulk remain intact. The growth of Al_2O_3 on the surface is shown in the higher magnification images at the bottom of Fig. 12b-c. Notably, the Al_2O_3 layer grown on the aluminized P91 after 5000 h at 700 °C, with a thickness of 4–9 μm, is thicker than the 2–5 μm layer formed after 5000 h at 600 °C. Despite the decrease in Al content in the coating below the oxide layer during exposure at 600 and 700 °C, continuous protection by a stable, slowly growing alumina scale was observed for exposures up to 5000 h to liquid Pb containing ~2×10^{-7} wt% dissolved oxygen. This is in contrast to a corrosion study of aluminized T91 in liquid Pb-Bi eutectic with an oxygen content below 10^{-8} wt%, where the oxygen activity was not sufficient to form a protective scale at 600 °C and dissolution corrosion was observed [15].

The corrosion resistance of aluminide coatings in stagnant liquid Pb depends greatly on their ability to form and sustain an alumina scale for longer exposure durations. Here the initial Al activity at the surface plays an important role together with the oxygen content in liquid Pb.

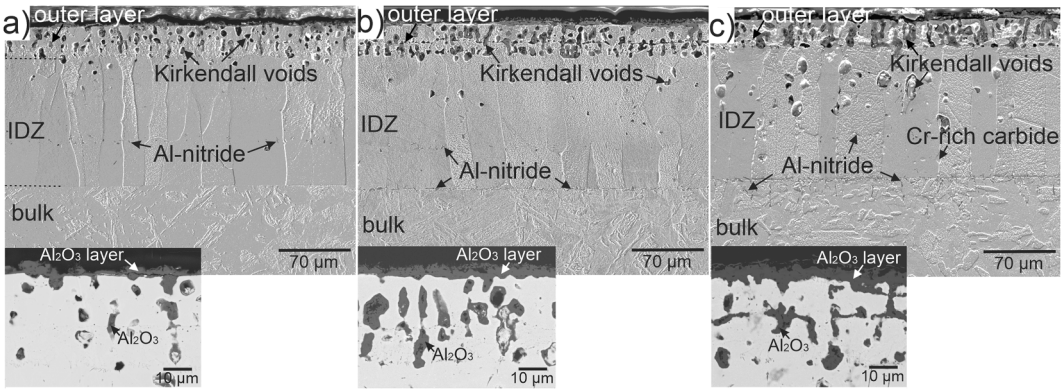

Fig. 12. SEM images of aluminized P91 after etching and its corresponding unetched images in higher magnification: a) initial state, i.e., after aluminizing and heat treatment procedure, b) after 5000 h exposure at 600 °C, and c) after 5000 h exposure at 700 °C.

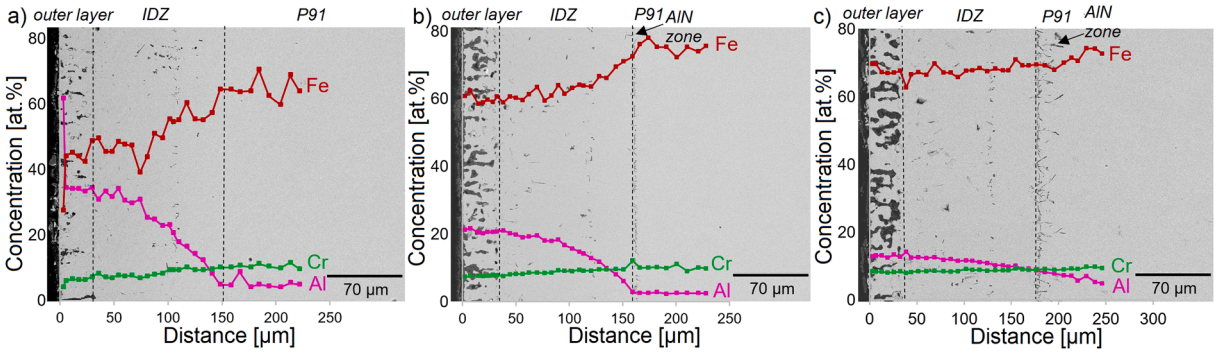

Fig. 13. EDS elemental line scan result of aluminized P91: a) initial state, b) after 5000 h exposure at 600 °C, and c) after 5000 h exposure at 700 °C.

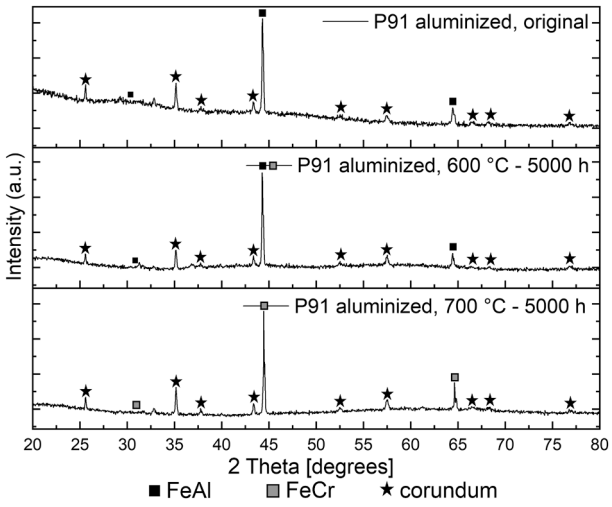

Fig. 14. XRD results of aluminized P91 before and after 5000 h exposures in liquid Pb.

Provided that these conditions enable the re-healing of a protective alumina scale (formed during heat treatment prior to Pb exposure in this case), the longevity of the coating then depends primarily on the interdiffusion with the substrate. Interdiffusion leads to Al depletion and Fe enrichment in the coating, which gradually transforms the coating from its intermetallic composition to an Al-containing solid solution structure with an increased Fe activity. This can be best observed by the shift of the interface between the coating and the substrate during exposure, in particular at 700 °C, and the decrease in Al content at the surface, see Fig. 13. As long as the Al content stays above ~8 wt%, depending on the Cr content, stable growth and self-healing of the protective alumina scale are expected [38,39]. Nevertheless, the reduced Al content can lead to the formation of Fe-containing mixed oxides for prolonged exposure, jeopardizing the corrosion resistance. Moreover, interdiffusion also leads to an increase in the extent of Kirkendall voids in the outer coating layer, providing pathways for the penetration of liquid Pb. Therefore, longer exposure studies are required to confirm the excellent corrosion protection of P91 by aluminide coatings.

4. Conclusion

In this study, the corrosion behavior in molten Pb was investigated for three different F/M steels (P91, 1.4748, 1.4136), one of them (P91) additionally coated with an aluminide pack cementation coating. Static exposure tests with duration up to 5000 h were performed at two different temperatures, 600 and 700 °C. In all tests, the molten Pb contained dissolved oxygen with a concentration of about 2×10^{-7} wt %. From the analysis of the exposed specimens after the tests, the following conclusions can be drawn:

- The martensitic steel P91, the material with the lowest Cr (~9 wt%) and C contents, shows the best corrosion resistance among the tested bulk materials. At both temperatures, an Fe-Cr spinel layer and inward-growing Cr_2O_3 are formed, which protect the steel from dissolution and Pb penetration even after 5000 h of exposure. However, Cr depletion due to the formation of the Cr-rich oxides occurs, which is most likely the reason for the ferritization of the martensite structure observed in surface-near regions.
- Aluminizing further improves the corrosion resistance of P91. During the heat treatment after pack cementation aimed at restoring the microstructure, an initial alumina scale formed on the coating surface. This alumina scale further grows during Pb exposure, providing a stable protection against corrosion even for prolonged exposure.
- The steel 1.4748 shows total dissolution and Pb penetration after prolonged exposure, despite the initial formation of an inward-growing Cr-Mn-rich oxide scale. The failure of the oxide scale and subsequent dissolution corrosion occurs earlier at 700 °C than at 600 °C. The inferior corrosion resistance of 1.4748 compared with P91 is attributed to its heterogeneous microstructure and the presence of Mn, both of which impede the formation of a uniform and stable oxide scale. The higher Cr content of 17.5 wt% compared with P91 is not beneficial, as large amounts of Cr are bound in Cr-carbides.
- The ferritic steel 1.4136 shows the formation of an oxide scale that is thinner and appears more stable and protective than the oxide formed on the surface of 1.4748. In addition to Cr and Mn, the scale contains substantial amounts of Si, which suggests a beneficial effect of Si on the corrosion resistance. Nevertheless, the scale becomes discontinuous after prolonged exposure, resulting in selective Cr dissolution and Pb penetration.
- Different corrosion patterns are observed for 1.4136 at the two investigated temperatures after prolonged exposure, which are correlated with the respective phase composition and microstructure of the bulk material at these temperatures. At 600 °C, an interconnected network of the Cr-rich σ-phase leads to a rather deep intergranular corrosion attack with dissolution of the σ-phase. At 700 °C, the Cr-rich phases are separated and the corrosion is less deep. Cr-rich carbides and σ-phase dissociate in surface-near regions due to Cr depletion.

CRediT authorship contribution statement

Alfons Weisenburger: Writing – review & editing, Supervision, Funding acquisition. **Ceyhun Oskay:** Writing – review & editing, Investigation. **Annette Heinzel:** Writing – review & editing, Investigation. **Georg Müller:** Resources, Project administration. **Renate Fetzer:** Writing – review & editing, Writing – original draft. **Anisa Purwitasari:** Writing – original draft, Visualization, Investigation.

Declaration of Competing Interest

The authors declare that they have no known competing financial interests or personal relationships that could have appeared to influence the work reported in this paper.

Acknowledgments

This research was funded by the German Federal Ministry for Economic Affairs and Climate Actions (BMWK) under the grant number 03EE5050C. The authors gratefully acknowledge Melanie Thalheimer for conducting the pack cementation and the post-coating heat treatment of Grade 91 steel.

Data availability

Data will be made available on request.

References

[1] E.A. Little, D.A. Stow, Void-swelling in irons and ferritic steels: II. An experimental survey of materials irradiated in a fast reactor, J. Nucl. Mater. 87 (1979) 25–39, https://doi.org/10.1016/0022-3115(79)90123-5.
[2] C. Cabet, F. Dalle, E. Gaganidze, J. Henry, H. Tanigawa, Ferritic-martensitic steels for fission and fusion applications, J. Nucl. Mater. 523 (2019) 510–537, https://doi.org/10.1016/j.jnucmat.2019.05.058.
[3] A. Alemberti, The lead fast reactor: an opportunity for the future? Engineering 2 (2016) 59–62, https://doi.org/10.1016/J.ENG.2016.01.022.
[4] A. Heinzel, W. Hering, J. Konys, L. Marocco, K. Litfin, G. Müller, J. Pacio, C. Schroer, R. Stieglitz, L. Stoppel, A. Weisenburger, T. Wetzel, Liquid metals as efficient high-temperature heat-transport fluids, Energy Technol. 5 (2017) 1026–1036, https://doi.org/10.1002/ente.201600721.
[5] Y. Kurata, M. Futakawa, S. Saito, Corrosion behavior of steels in liquid lead–bismuth with low oxygen concentrations, J. Nucl. Mater. 373 (2008) 164–178, https://doi.org/10.1016/j.jnucmat.2007.05.051.
[6] A. Doubková, F. Di Gabriele, P. Brabec, E. Keilová, Corrosion behavior of steels in flowing lead–bismuth under abnormal conditions, J. Nucl. Mater. 376 (2008) 260–264, https://doi.org/10.1016/j.jnucmat.2008.02.033.
[7] A. Heinzel, G. Müller, A. Weisenburger, Behavior of welds in liquid lead containing 10−6wt% and 10−8wt% oxygen, J. Nucl. Mater. 437 (2013) 116–121, https://doi.org/10.1016/j.jnucmat.2013.01.298.
[8] Z. Zhu, Q. Zhang, J. Tan, X. Wu, H. Ma, Z. Zhang, Q. Ren, E.-H. Han, X. Wang, Corrosion behavior of T91 steel in liquid lead-bismuth eutectic at 550 °C: effects of exposure time and dissolved oxygen concentration, Corros. Sci. 204 (2022) 110405, https://doi.org/10.1016/j.corsci.2022.110405.
[9] S. Tian, Y. Pang, Z. Jiang, L. Luo, Z. Xiao, Corrosion characteristics of T91 steel in lead–bismuth eutectic with different oxygen concentrations at 500°C, Mater. Corros. 73 (2022) 134–142, https://doi.org/10.1002/maco.202112505.
[10] A. Weisenburger, A. Heinzel, G. Müller, H. Muscher, A. Rousanov, T91 cladding tubes with and without modified FeCrAlY coatings exposed in LBE at different flow, stress and temperature conditions, J. Nucl. Mater. 376 (2008) 274–281, https://doi.org/10.1016/j.jnucmat.2008.02.026.
[11] G. Müller, G. Schumacher, F. Zimmermann, Investigation on oxygen controlled liquid lead corrosion of surface treated steels, J. Nucl. Mater. 278 (2000) 85–95, https://doi.org/10.1016/S0022-3115(99)00211-1.
[12] A. Heinzel, M. Kondo, M. Takahashi, Corrosion of steels with surface treatment and Al-alloying by GESA exposed in lead–bismuth, J. Nucl. Mater. 350 (2006) 264–270, https://doi.org/10.1016/j.jnucmat.2006.01.014.
[13] E. Miorin, F. Montagner, V. Zin, D. Giuranno, E. Ricci, M. Pedroni, V. Spampinato, E. Vassallo, S.M. Deambrosis, Al rich PVD protective coatings: a promising approach to prevent T91 steel corrosion in stagnant liquid lead, Surf. Coat. Technol. 377 (2019) 124890, https://doi.org/10.1016/j.surfcoat.2019.124890.
[14] A. Heinzel, R. Fetzer, F. Lang, A. Weisenburger, S. Cataldo, F. Di Fonzo, G. Müller, Corrosion tests on austenitic samples with alumina and alumina-forming coatings in oxygen-containing stagnant Pb and turbulently flowing PbBi, J. Nucl. Mater. 596 (2024) 155121, https://doi.org/10.1016/j.jnucmat.2024.155121.
[15] Ph Deloffre, F. Balbaud-Célérier, A. Terlain, Corrosion behaviour of aluminized martensitic and austenitic steels in liquid Pb–Bi, J. Nucl. Mater. 335 (2004) 180–184, https://doi.org/10.1016/j.jnucmat.2004.07.014.
[16] A. Naji, M.C. Galetz, M. Schütze, Design model for diffusion coatings formed via pack cementation, Mater. Corros. 65 (2014) 312–318, https://doi.org/10.1002/maco.201307393.
[17] C. Oskay, T.M. Meißner, C. Dobler, B. Grégoire, M.C. Galetz, Scale formation and degradation of diffusion coatings deposited on 9% Cr steel in molten solar salt, Coatings 9 (2019), https://doi.org/10.3390/coatings9100687.
[18] A. Agüero, R. Muelas, M. Gutiérrez, R. Van Vulpen, S. Osgerby, J.P. Banks, Cyclic oxidation and mechanical behaviour of slurry aluminide coatings for steam turbine components, Surf. Coat. Technol. 201 (2007) 6253–6260, https://doi.org/10.1016/j.surfcoat.2006.11.033.
[19] V. Rohr, M. Schütze, Novel low temperature diffusion coatings for heat exchanger materials, Mater. Sci. Forum 461–464 (2004) 401–408, https://doi.org/10.4028/www.scientific.net/MSF.461-464.401.
[20] A. Agüero, V. González, R. Muelas, Diffusion stable aluminide coatings: Behaviour under steam and oxy-fuel fire-side conditions at 650 °C and accelerated diffusion tests at 900 °C, Surf. Coat. Technol. 350 (2018) 119–127, https://doi.org/10.1016/j.surfcoat.2018.07.027.
[21] C. Pandey, A. Giri, M.M. Mahapatra, Evolution of phases in P91 steel in various heat treatment conditions and their effect on microstructure stability and mechanical properties, Mater. Sci. Eng. A 664 (2016) 58–74, https://doi.org/10.1016/j.msea.2016.03.132.
[22] C. Pandey, M.M. Mahapatra, P. Kumar, N. Saini, Homogenization of P91 weldments using varying normalizing and tempering treatment, Mater. Sci. Eng. A 710 (2018) 86–101, https://doi.org/10.1016/j.msea.2017.10.086.
[23] B.L. Bates, Y. Zhang, S. Dryepondt, B.A. Pint, Creep behavior of pack cementation aluminide coatings on Grade 91 ferritic–martensitic alloy, Surf. Coat. Technol. 240 (2014) 32–39, https://doi.org/10.1016/j.surfcoat.2013.12.008.
[24] Handbook on Lead-bismuth Eutectic Alloy and Lead Properties, Materials Compatibility, Thermal-hydraulics and Technologies, OECD Publishing, Paris, 2015.
[25] A. Baltušnikas, A. Grybėnas, R. Kriūkienė, I. Lukošiūtė, V. Makarevičius, Evolution of crystallographic structure of M23C6 carbide under thermal aging of P91 steel, J. Mater. Eng. Perform. 28 (2019) 1480–1490, https://doi.org/10.1007/s11665-019-03935-1.
[26] C. Schroer, V. Koch, O. Wedemeyer, A. Skrypnik, J. Konys, Silicon-containing ferritic/martensitic steel after exposure to oxygen-containing flowing lead–bismuth eutectic at 450 and 550 °C, J. Nucl. Mater. 469 (2016) 162–176, https://doi.org/10.1016/j.jnucmat.2015.11.058.
[27] H. Shi, H. Wang, R. Fetzer, A. Heinzel, A. Weisenburger, K. Wang, A. Jianu, G. Müller, Influence of Si addition on the corrosion behavior of 9 wt% Cr ferritic/martensitic steels exposed to oxygen-controlled molten Pb-Bi eutectic at 550 and 600 °C, Corros. Sci. 193 (2021) 109871, https://doi.org/10.1016/j.corsci.2021.109871.
[28] Q. Chen, L. Zhai, Y. Chen, H. Liu, J. Yang, F. Zhang, Corrosion behaviour of 11Cr1Si ferritic/martensitic steel in static liquid lead–bismuth eutectic at 450–550 ℃, Nucl. Mater. Energy 35 (2023) 101429 https://doi.org/10.1016/j.nme.2023.101429.
[29] M. Zhang, G. He, R. Scales, K. Song, M. Lapington, W. Zhou, Z. Ding, M.P. Short, P. A.J. Bagot, M.P. Moody, F. Hofmann, Correlated chromium carbide dissociation and phase transformation in liquid lead-bismuth eutectic corroded T91 steel, Corros. Sci. 249 (2025) 112851, https://doi.org/10.1016/j.corsci.2025.112851.
[30] X. Jin, S. Chen, L. Rong, Effects of Mn on the mechanical properties and high temperature oxidation of 9Cr2WVTa steel, J. Nucl. Mater. 494 (2017) 103–113, https://doi.org/10.1016/j.jnucmat.2017.07.024.
[31] Z. Dong, M. Li, Y. Behnamian, J.-L. Luo, W. Chen, B.S. Amirkhiz, P. Liu, X. Pang, J. Li, W. Zheng, D. Guzonas, C. Xia, Effects of Si, Mn on the corrosion behavior of ferritic–martensitic steels in supercritical water (SCW) environments, Corros. Sci. 166 (2020) 108432, https://doi.org/10.1016/j.corsci.2020.108432.
[32] W. Zeng, M. Zhou, M. Yang, R. Qiu, X. Tan, A. Zhou, X. Luo, Influence of manganese content on microstructure, mechanical properties and high temperature oxidation resistance of reduced activation ferritic/martensitic steels, J. Mater. Eng. Perform. 32 (2023) 9765–9776, https://doi.org/10.1007/s11665-023-07831-7.
[33] L. Niewolak, L. Garcia-Fresnillo, G.H. Meier, W.J. Quadakkers, Sigma-phase formation in high chromium ferritic steels at 650°C, J. Alloy. Compd. 638 (2015) 405–418, https://doi.org/10.1016/j.jallcom.2015.03.076.
[34] Y. Zhang, B.A. Pint, K.M. Cooley, J.A. Haynes, Formation of aluminide coatings on Fe-based alloys by chemical vapor deposition, Surf. Coat. Technol. 202 (2008) 3839–3849, https://doi.org/10.1016/j.surfcoat.2008.01.023.
[35] A. Purwitasari, R. Fetzer, A. Heinzel, C. Oskay, A. Weisenburger, G. Müller, Influence of aluminizing and pre-oxidation on corrosion behavior of 316Ti in liquid Pb at 600–700 °C, Corros. Sci. 251 (2025) 112896, https://doi.org/10.1016/j.corsci.2025.112896.
[36] S. Majumdar, A. Borgohain, V. Kain, Interaction between liquid lead-bismuth eutectic and aluminized Inconel 625 superalloy at 600 and 850 °C, J. Nucl. Mater. 518 (2019) 54–61, https://doi.org/10.1016/j.jnucmat.2019.02.046.
[37] B.A. Pint, Y.-F. Su, M.P. Brady, Y. Yamamoto, J. Jun, M.R. Ickes, Compatibility of alumina-forming austenitic steels in static and flowing Pb, JOM 73 (2021) 4016–4022, https://doi.org/10.1007/s11837-021-04961-y.
[38] R. Fetzer, A. Weisenburger, A. Jianu, G. Müller, Oxide scale formation of modified FeCrAl coatings exposed to liquid lead, Corros. Sci. 55 (2012) 213–218, https://doi.org/10.1016/j.corsci.2011.10.019.
[39] A. Jianu, R. Fetzer, A. Weisenburger, S. Doyle, M. Bruns, A. Heinzel, P. Hosemann, G. Mueller, Stability domain of alumina thermally grown on Fe–Cr–Al-based model alloys and modified surface layers exposed to oxygen-containing molten Pb, J. Nucl. Mater. 470 (2016) 68–75, https://doi.org/10.1016/j.jnucmat.2015.12.009.